GEOPHYSICS, VOL. 71, NO. 4 (JULY-AUGUST 2006); P. U47–U57, 28 FIGS., 1 TABLE.
10.1190/1.2210969

Early arrival waveform tomography on near-surface refraction data

Jianming Sheng[1], Alan Leeds[2], Maike Buddensiek[1], and Gerard T. Schuster[1]

ABSTRACT

We develop a waveform-tomography method for estimating the velocity distribution that minimizes the waveform misfit between the predicted and observed early arrivals in space-time seismograms. By fitting the waveforms of early arrivals, early arrival waveform tomography (EWT) naturally takes into account more general wave-propagation effects compared to the high-frequency method of traveltime tomography, meaning that EWT can estimate a wider range of slowness wavenumbers. Another benefit of EWT is more reliable convergence compared to full-waveform tomography, because an early-arrival misfit function contains fewer local minima. Synthetic test results verify that the waveform tomogram is much more accurate than the traveltime tomogram and that this algorithm has good convergence properties. For marine data from the Gulf of Mexico, the statics problem caused by shallow, gassy muds was attacked by using EWT to obtain a more accurate velocity model. Using the waveform tomogram to correct for statics, the stacked section was significantly improved compared to using the normal moveout (NMO) velocity, and moderately improved compared to using the traveltime tomogram. Inverting high-resolution land data from Mapleton, Utah, showed an EWT velocity tomogram that was more consistent with the ground truth (trench log) than the traveltime tomogram. Our results suggest that EWT can provide supplemental, shorter-wavelength information compared to the traveltime tomogram for both shallow and moderately deep seismic data.

INTRODUCTION

Traveltime tomography is a geophysical imaging tool that inverts the traveltimes of seismic arrivals for the earth's velocity structure (Aki and Richards, 2002). The velocity model is updated by iteratively back-projecting the traveltime residuals along rays. It is cost efficient, somewhat robust, and has long been a standard for delineating the earth's velocity distribution. However, traveltime tomography assumes that the data are high-frequency, which conflicts with the finite-frequency bandwidth of the seismic source and results in a suboptimal estimate of the earth's velocity field.

To overcome this high-frequency limitation, much effort has been focused on fat-ray or Fresnel-volume tomography (Červený and Soares, 1992; Schuster and Quintus-Bosz, 1993; and Vasco et al., 1995) and full-waveform inversion including Lailly (1984), Tarantola (1984, 1987), and Mora (1987, 1988), by which multiple paths and multiple arrivals also can be taken into account. Waveform inversion can be implemented in the frequency domain (Pratt, 1990; Pratt et al., 1996 and 1998; Liao and McMechan, 1996; Shipp and Singh, 2002) or time domain (Tarantola, 1986; Mora, 1987; Zhou et al., 1995 and 1997; Wang, 1995; Bunks et al., 1995). Numerical results verified that waveform inversion can reconstruct a much more accurate velocity model than traveltime inversion, partly because it does not require a high-frequency approximation. However, the full-waveform misfit function is highly nonlinear, which can result in poor convergence properties and has the tendency to get stuck in one of many local minima (Gauthier et al., 1986).

To stabilize the inversion, it was advocated to apply a time window to the early arrivals (Pratt and Worthington, 1988). Here, early arrivals are defined as those events that arrive within a few periods of the first arrivals. With the early arrival time window, the misfit function is not populated densely by local minima as is the case in the misfit function for full-waveform tomography. This idea is illustrated in Figure 1, in which Figure 1a–c shows the full waveforms, early arrivals, and traveltimes for a two-layer earth model, and Figure 1d–f shows the corresponding plots of misfit functions versus hypothetical velocities. The early arrival waveform misfit function in Figure 1e shows many fewer local minima compared to that for the full-waveform misfit function, so there are fewer convergence problems.

The early arrival waveform tomography (EWT) method applies the early arrival time window in the time domain, which is more convenient compared to the frequency-domain methods. With the traveltime tomogram as a good estimate of the low-wavenumber velocity model (Luo and Schuster, 1991), EWT can yield highly resolved

Manuscript received by the Editor June 29, 2004; revised manuscript received December 1, 2005; published online July 12, 2006.
[1]University of Utah, Department of Geology and Geophysics, Salt Lake City, Utah 84112. E-mail: jsheng_2004@yahoo.com; maikeb@gfz-potsdam.de; schuster@mines.utah.edu.
[2]ChevronTexaco, ChevronTexaco Energy Technology Company, 4800 Fournace Place, Bellaire, Texas, 77401. E-mail: AlanLeeds@chevrontexaco.com.

velocity models because no high-frequency assumption is required, and it also has more reliable convergence properties compared to full-waveform tomography.

This paper first presents the theory of EWT. We then apply EWT to 2D synthetic data, marine data, and land data from a refraction survey, respectively. Finally, a summary of results is presented.

THEORY

To simplify the computations, we assume that early arrivals honor the acoustic-wave equation given by

$$\frac{1}{\kappa(\mathbf{r})}\frac{\partial^2 p(\mathbf{r},t|\mathbf{r}_s)}{\partial t^2} - \nabla \cdot \left[\frac{1}{\rho(\mathbf{r})}\nabla\, p(\mathbf{r},t|\mathbf{r}_s)\right] = s(\mathbf{r},t|\mathbf{r}_s), \tag{1}$$

where $p(\mathbf{r},t|\mathbf{r}_s)$ denotes the pressure at time t at the receiver $\mathbf{r}$ because of a source at $\mathbf{r}_s$; $\kappa(\mathbf{r})$ and $\rho(\mathbf{r})$ are the bulk modulus and density functions, respectively; and $s(\mathbf{r},t|\mathbf{r}_s)$ is the source function. These parameters can be used to generate synthetic seismograms by a fourth-order, finite-difference method (Levander, 1988).

Fortunately, ignoring shear-wave effects by simplification to the acoustic-wave equation still allows waveform tomography to sometimes estimate highly resolved models of the earth, as demonstrated in the waveform-tomography study of Zhou et al. (1995). EWT estimates the velocity model $c(\mathbf{x}) = \sqrt{\kappa(\mathbf{x})/\rho(\mathbf{x})}$ by minimizing the early arrival waveform misfit function

$$E = \frac{1}{2}\sum_s \sum_r \int dt(\delta p_{rs}(t))^2, \tag{2}$$

where the waveform residual $\delta p_{rs}(t)$ is defined as

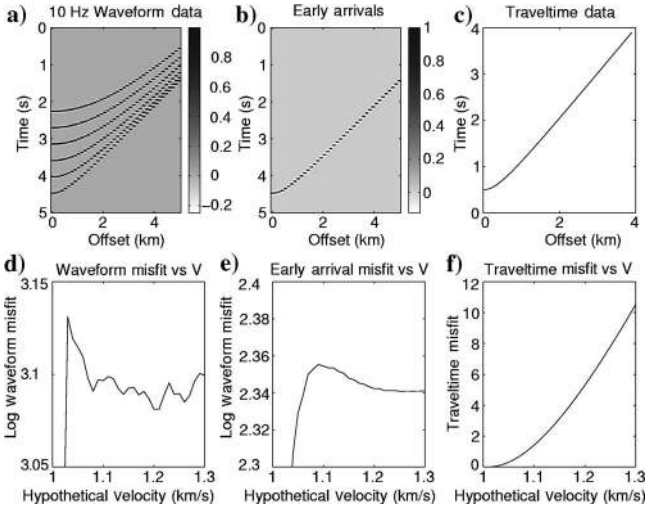

Figure 1. (a) CSG seismograms $p_{obs}(x,t)$ for a two-layer earth model with a rigid surface. Note that the PP primary reflection energy is followed by five multiple reflection arrivals, and the direct wave has been muted. (b) Early arrivals used for EWT. (c) Associated PP traveltime $t_{obs(x)}$ curve. (d) Full-waveform misfit function $\epsilon = \Sigma_t\Sigma_x[p_{pred}(x,t) - p_{obs}(x,t)]^2$ plotted against different values of the hypothetical velocity V of the first layer. The correct value of V is 1.0 km/s. (e) Early arrival misfit function versus the hypothetical velocity V. (f) Traveltime misfit function $\epsilon = \Sigma_x[t_{pred}(x) - t_{obs}(x)]^2$.

$$\delta p_{rs}(t) = [p(\mathbf{r},t|\mathbf{r}_s)_{obs} - p(\mathbf{r},t|\mathbf{r}_s)_{cal}]m(\mathbf{r}_s,\mathbf{r},t). \tag{3}$$

Here, $p(\mathbf{r},t|\mathbf{r}_s)_{obs}$ and $p(\mathbf{r},t|\mathbf{r}_s)_{cal}$ denote the observed and calculated seismic traces, respectively, and $m(\mathbf{r}_s,\mathbf{r},t)$ is a mute function that mutes all energy except for the early arrivals. The notation for the source-initiation time t_s is suppressed because the source is always initiated at $t_s = 0$.

A preconditioned conjugate-gradient method (Luo and Schuster, 1991) is used to minimize the misfit function. The preconditioning term $\mathbf{P}$ is the diagonal inverse to the Hessian, and the velocity model is updated recursively using search directions defined by

$$\mathbf{d}_k = -\mathbf{P}_k\mathbf{g}_k + \beta_k\mathbf{d}_{k-1}, \tag{4}$$

for iterations $k = 1,2,\ldots$, with $\mathbf{d}_0 = -\mathbf{g}_0$. The velocity model is updated by

$$c_{k+1}(\mathbf{x}) = c_k(\mathbf{x}) + \lambda_k d_k(\mathbf{x}), \tag{5}$$

where λ_k is the step length, $\mathbf{d} = \{d(\mathbf{x})$ for all image points $\mathbf{x}$ in the model$\}$, and $\mathbf{g} = \{g(\mathbf{x})$ for all image points $\mathbf{x}$ in the model$\}$. The misfit gradient $\mathbf{g}_k$ at iteration k is given by $g_k(\mathbf{x}) = \partial E_k/\partial c_k(\mathbf{x})$ for all image points $\mathbf{x}$. The parameter β_k is computed by the Polak-Ribiére formula (Nocedal and Wright, 1999)

$$\beta_k = \frac{\mathbf{g}_k^T \cdot (\mathbf{P}_k\mathbf{g}_k - \mathbf{P}_{k-1}\mathbf{g}_{k-1})}{\mathbf{g}_{k-1}^T \cdot \mathbf{P}_{k-1}\mathbf{g}_{k-1}}. \tag{6}$$

The starting model $c_0(\mathbf{x})$ is obtained from the traveltime tomogram in order to supply the low-wavenumber estimate of the velocity model. The gradient can be computed by the zero-lag correlation between the forward-propagated wavefield and the back-projected wavefield of the waveform residuals (Tarantola, 1987; Mora, 1987; Luo and Schuster, 1991; Crase et al., 1992; Woodward, 1992; and Zhou et al., 1995 and 1997),

$$g(\mathbf{x}) = \frac{1}{c^3(\mathbf{x})}\sum_s \sum_r \int dt\, m(\mathbf{r}_s,\mathbf{r},t)\dot{p}(\mathbf{x},t|\mathbf{r}_s)_{cal}\dot{p}_b(\mathbf{x},t|\mathbf{r},\mathbf{r}_s), \tag{7}$$

where $\dot{p}$ denotes the time derivative of p, and $p_b(\mathbf{x},t|\mathbf{r},\mathbf{r}_s)$ represents the back-projected wavefield of the waveform residuals given by

$$p_b(\mathbf{x},t|\mathbf{r},\mathbf{r}_s) = G(\mathbf{x},t|\mathbf{r},0) * \delta p_{rs}(t)m(\mathbf{r}_s,\mathbf{r},t), \tag{8}$$

where $G(\mathbf{x},t|\mathbf{r},0)$ is the Green's function associated with equation 1 for the velocity field $c(\mathbf{x})$, and the symbol $*$ represents temporal convolution. Equation 5 is applied iteratively until the misfit-function value satisfies some stopping criterion.

DATA PREPROCESSING

The starting model for EWT is the traveltime tomogram. Thus, the first-arrival traveltimes need to be picked and inverted for $c_0(\mathbf{x})$. The next step is to process the traces before the application of EWT in order to account for limitations in modeling elastic-field data by numerical solutions to the acoustic-wave equation. These processing steps include accounting for 3D geometrical spreading, radiation patterns, and the source wavelet. The following steps describe the implementation of EWT:

- The field data are transformed from 3D to 2D by applying the fil-

ter $\sqrt{i/\omega}$ in the frequency domain and scaling the data by $\sqrt{t}$ to approximate geometrical spreading (Barton, 1989; Zhou et al., 1995);

- Because the forward modeling is based on the acoustic-wave equation, the nonacoustic factors should be dealt with prior to waveform inversion. The critical step is to correct for attenuation. According to Liao and McMechan (1997), the linear attenuation-transfer function $T(f)$ relates the input $S(f)$ signal spectrum to that of the output trace $R(f) = T(f)S(f)$, with

$$T(f) = \exp\left\{-f\frac{\pi t}{Q}\right\}, \tag{9}$$

where the attenuation factor Q is assumed to be constant, and t denotes the first-arrival traveltime. The factor Q is also related to the centroid frequency defined as

$$f_r = f_s - \frac{2\pi\sigma_s^2}{Q}t, \tag{10}$$

where f_r and f_s denote the centroid frequencies at the receiver and the source, separately, and σ_s^2 denotes the variance of the source spectrum. After f_r and σ_s^2 are estimated from the data and the traveltimes t are picked, the Q value can be estimated by a line-fit procedure (Wang, 1995). With the estimated Q value, the attenuation effects can be corrected approximately according to equation 9.

- The traces are then normalized to reduce the errors resulting from the estimated Q values and the geometrical-spreading correction; the traces are then muted to retain only the early arrivals. The length of the time window can be a few periods, such that surface waves or other unpredicted waves are not included.
- Traveltimes are picked and inverted by traveltime tomography to obtain a good initial-velocity model.
- The source wavelet is estimated by back-projecting the near-offset waveform residuals (Zhou et al., 1995) or, in some cases, just averaging the first arrivals. The radiation pattern of the source is accounted for by an appropriate source term in the finite-difference (FD) solution of the wave equation (Wang, 1995).
- A fourth-order, FD solution to the 2D acoustic-wave equation (Levander, 1988) with perfectly matched layer (PML) boundary conditions (Berenger, 1994; Chew and Liu, 1996; Zeng et al., 2001; and Festa and Nielsen, 2003) is used to compute the predicted arrivals. The waveform-gradient method of Zhou et al. (1995) with a preconditioned conjugate-gradient algorithm is used to compute the updated velocity in equation 5 until the predicted early arrival waveforms satisfactorily match those of the data. The criterion for satisfactory waveform matching is such that the misfit function decreases by less than 0.1% for several iterations.

NUMERICAL TESTS

The EWT algorithm was applied to three data sets: 2D synthetic data; 2D Gulf of Mexico marine data; and 2D near-surface refraction data recorded over the Wasatch fault near Mapleton, Utah. The goal of these tests was to verify that EWT provides a robust estimate of the earth's velocity distribution that is significantly more accurate than that estimated from the traveltime tomogram.

2D synthetic data

Figure 2 shows a 2D model with a sinusoidal interface (model suggested by Konstantin Osypov from WesternGeco). This survey was designed to test the resolution of the waveform tomogram, in which the dominant-source wavelength is 40 m, the wavelength of the sine curve is 10 m, and the amplitude is 5 m. Twenty-one sources and 51 geophones are evenly located on the surface with source and geophone intervals of 10 m and 4 m, respectively. An acoustic, fourth-order, FD code was used to generate the seismograms with a sample length of 0.15 s; a 60-Hz peak frequency Ricker wavelet is the source wavelet. Figure 3 shows the 10th common-shot gather (CSG). The dominant-source wavelength at the undulating interface is estimated to be about 40 m, which violates the high-frequency assumption of ray tracing (Bleistein et al., 2001) for a 60-Hz source. The computational grid dimension is 401 × 121 grid points, and each simulation required 1500 time steps.

Shot gathers were generated by the FD method, and the first-arrival traveltimes were used as input into array-based, traveltime-tomography code that uses a multiscale smoothing procedure (Nemeth et al., 1997). Different smoothing schedules were employed, as shown in Table 1, where a large smoothing filter with 40 × 30 (20 × 15 m) grid points was used to smooth the tomogram for the first five iterations. Then the filter dimensions were decreased gradually to 16 × 10 (8 × 5 m) grid points for the last 15 iterations. Roughly

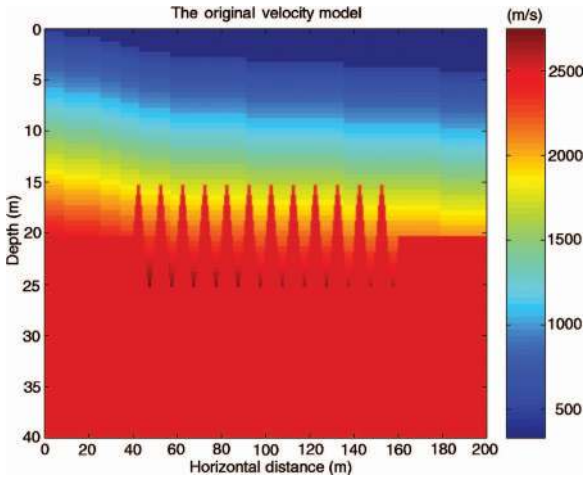

Figure 2. 2D model with a sinelike interface suggested by Konstantin Osypov.

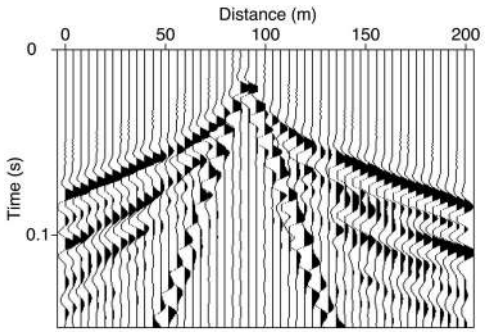

Figure 3. The 10th CSG of the synthetic data. Here, the first-arrival window was 20 ms wide and started at the first-break traveltime.

speaking, starting the iterations with coarse smoothing filters often leads to rapid progress to the global minima and tends to avoid local minima (Nemeth et al., 1997) in the misfit function.

Figure 4 shows the traveltime tomogram (top) and EWT tomogram (bottom); in this case, no ground roll or mode conversions, attenuation, 3D effects, or anisotropy effects were considered. Here, a 0.02-s time window and trace normalization were applied to the data. The results show that traveltime tomography recovers the long-wavelength features, but the short-wavelength details are blurred. In contrast, the EWT tomogram provides a very accurate estimate of both the coarse and finely detailed features in the actual model. Unlike EWT, the ray-based tomogram is poorly resolved, because the high-frequency assumption of ray-based tomography is violated with this model. EWT also accounts for any diffraction effects that might distort the phase or amplitude of the early arrivals. Figure 5 depicts the plots of traveltime residual (top) and waveform residual (bottom) versus iteration number and shows that the traveltime tomogram accurately predicts the traveltimes within a tolerance of 0.3 ms. The waveform data predicted from the waveform tomogram predict every arrival almost exactly (not shown), which explains and is consistent with the rapid convergence of the waveform residual seen in Figure 5.

Table 1. The smoothing schedule for synthetic data.

Smoothing size (in grid points)	Iterations	Grid size (m)	RMS residual (ms)
40 × 30	5	0.5	3.65
30 × 20	5	0.5	2.55
20 × 15	5	0.5	1.24
16 × 10	15	0.5	0.31

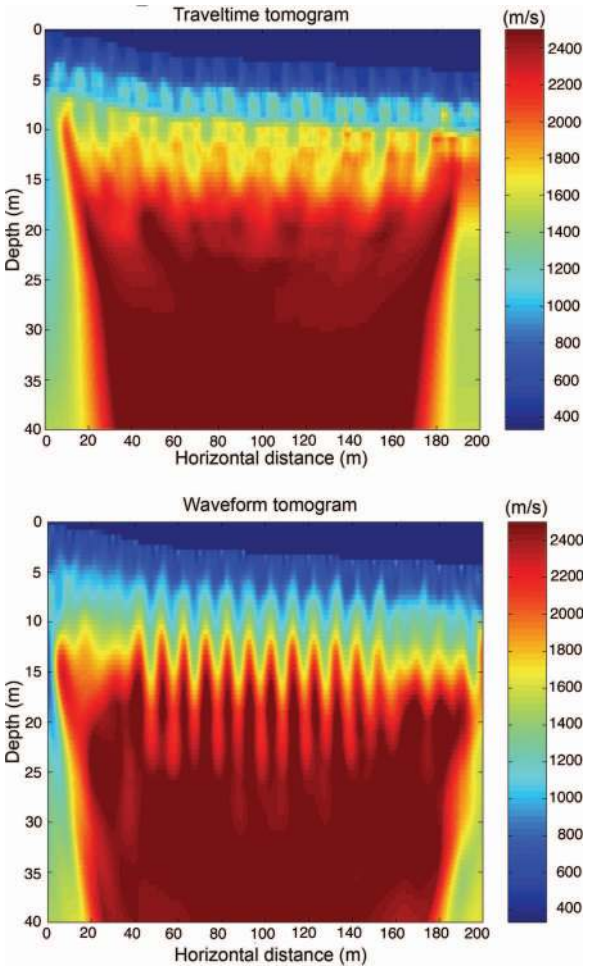

Figure 4. Velocity tomograms obtained by a (top) ray-based tomography method and (bottom) EWT. The EWT tomogram accurately resolves finer-detailed features of the model, while the traveltime tomogram smears the finely detailed features.

2D ChevronTexaco's Gulf of Mexico data

This 2D marine data set (courtesy of ChevronTexaco, with permission from WesternGeco) consists of 990 shots with a shot interval of 25 m, a time-sample interval of 4 ms, a trace length of 8188 ms, and 180 active hydrophones per shot. The receiver spacing is 25 m with a near offset of 173 m and a far offset of 4648 m. Figure 6 shows the NMO stacked section. From the white boxes, it can be seen that some velocity variations resulting from shallow, gassy muds (which were observed in well-log data) cause time sags and false structures. The objective here is to invert the first-arrival data by both traveltime tomography and EWT and determine which method gives the best statics corrections.

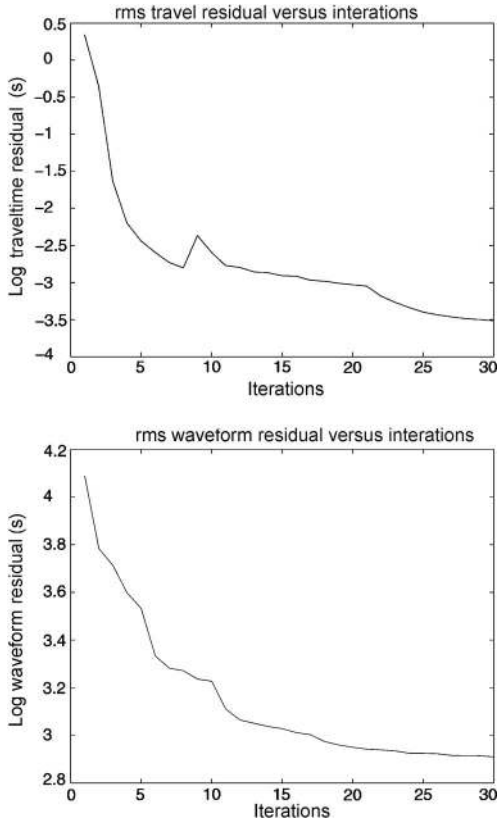

Figure 5. The traveltime residual (top) and waveform residual (bottom) versus iterations for the traveltime-tomography and EWT methods.

Traveltime tomostatics + residual statics

Traveltime tomostatics and residual statics can be calculated with the following steps:

- A total of 490 × 177 = 86,730 first-arrival traveltimes were picked using an automatic picking code and were inverted by traveltime tomography. Figure 7 shows a typical gather (from shot 663), with the solid curve indicating the picked traveltimes. Figure 8 shows the traveltime-velocity tomogram, and Figures 9 and 10 show the ray-density distribution and the refraction-migration image (Zhang, 1996), respectively. The tomogram re-

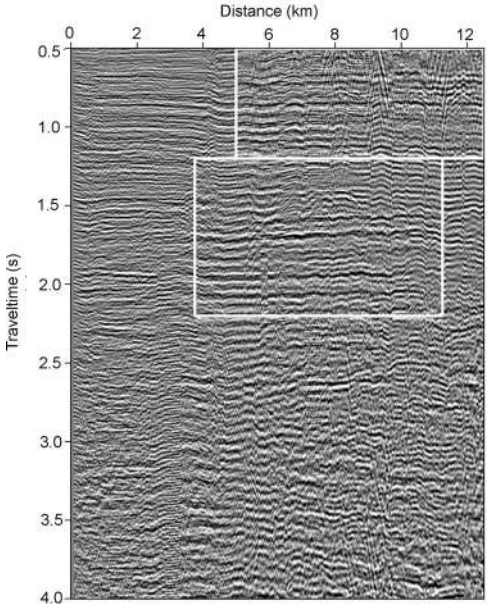

Figure 6. The stacked section using the NMO velocity.

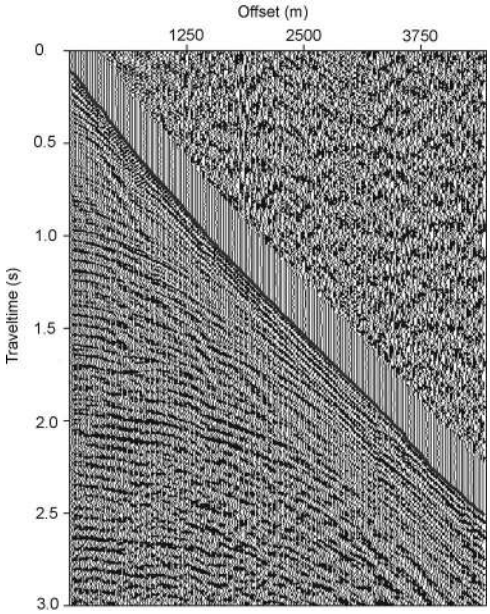

Figure 7. The CSG for shot 663. The solid dark curve indicates the picked traveltimes.

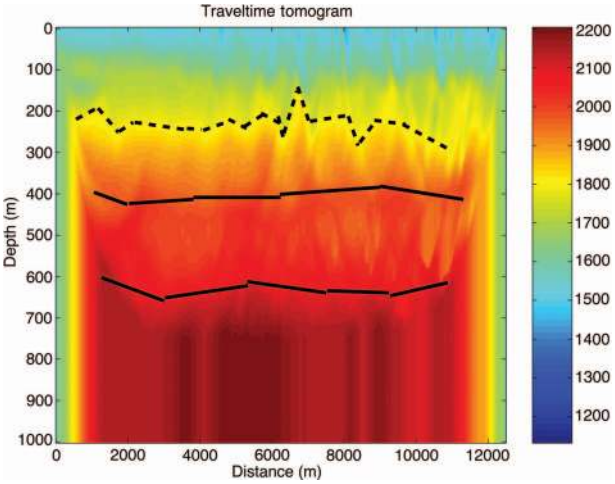

Figure 8. The traveltime-velocity tomogram (velocity in m/s) for the 2D marine data. The dashed contour delineates the shallow low-velocity zone, and the solid lines indicate the interpreted refractors.

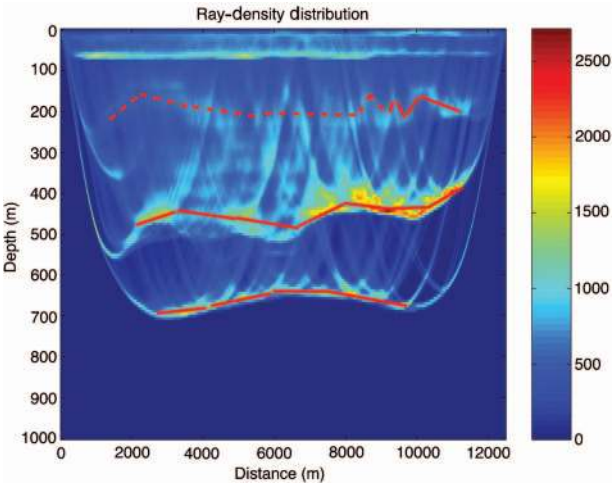

Figure 9. This shows the ray-density distribution for the traveltime tomography.

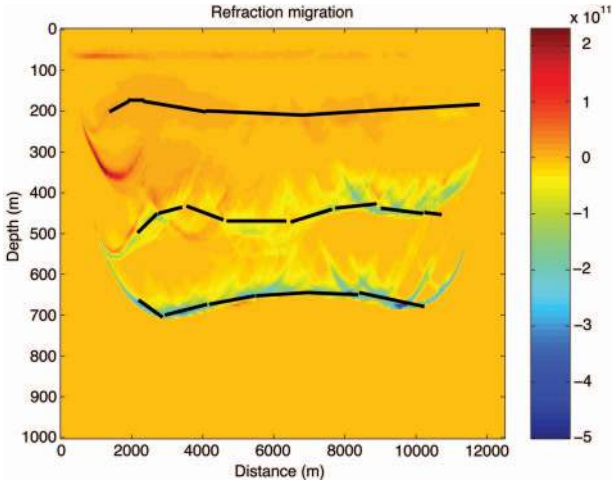

Figure 10. The refraction-migration image using the traveltime tomogram as the migration velocity model.

solved some shallow, low-velocity zones along the dashed contours.

- The traveltime tomogram was used to estimate the source and receiver statics (Zhu et al., 1992) vertically from the surface downward to a datum of 400 m and then upward to the surface using a constant-substitute velocity. These corrections will be denoted as traveltime tomostatics, and similarly the statics estimated with the waveform tomogram will be denoted as waveform tomostatics.
- After the traveltime-tomostatics corrections, reflection-residual statics (Rothman, 1985 and 1986; Zhu et al., 1992; Marsden, 1993; Wilson et al., 1994; Taner et al., 1998), were calculated for reflections in the time window from 0.8 to 2.0 s. The stacked section was obtained, shown in Figure 11, after application of traveltime tomostatics, followed by reflection-residual statics. Compared with the NMO stacked section in Figure 6, the quality of the stacked section after tomostatics and residual-statics corrections is improved noticeably (see Figure 12 for a zoom view).

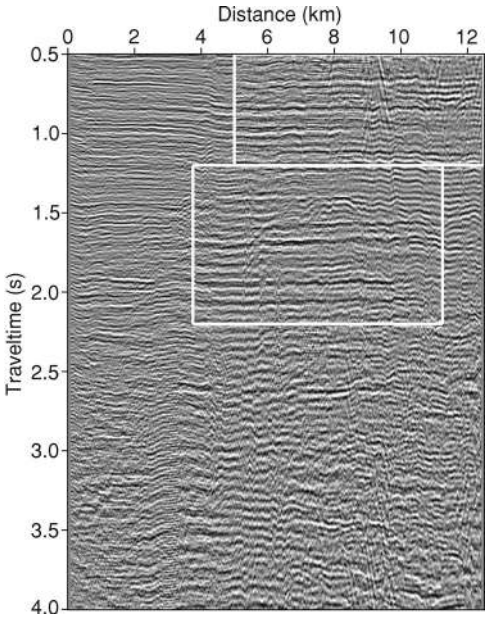

Figure 11. The stacked section after traveltime-tomostatics and reflection-residual statics corrections using the traveltime tomogram. Compared to the NMO stacked section shown in Figure 6, the traveltime stacked section shows improvement in the strength and lateral continuity of reflectors, which can be seen more clearly in the zoom view of the two white boxes in Figure 12.

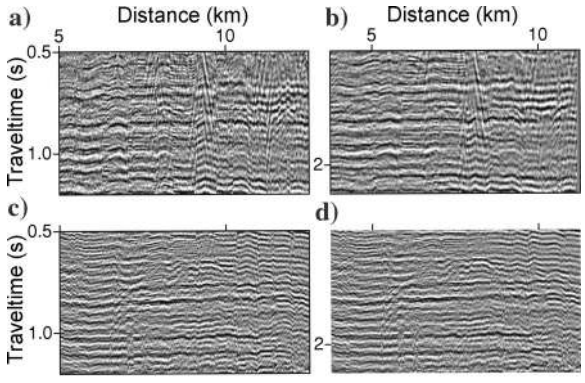

Figure 12. The zoom views for the upper white box in the stacked sections using the (a) NMO velocity and (b) traveltime tomogram; (c) and (d) show the zoom views for the lower white box in the same order.

EWT statics + residual statics

Can statics corrections with a velocity model estimated by waveform tomography provide an even more accurate stacked section? To answer this question, the velocity model was estimated by EWT, and the resulting tomostatics corrections were applied to the reflection data. This procedure was performed using the following steps:

- Following the processing procedure described in a previous section, the Q value was estimated, and the attenuation effects in the

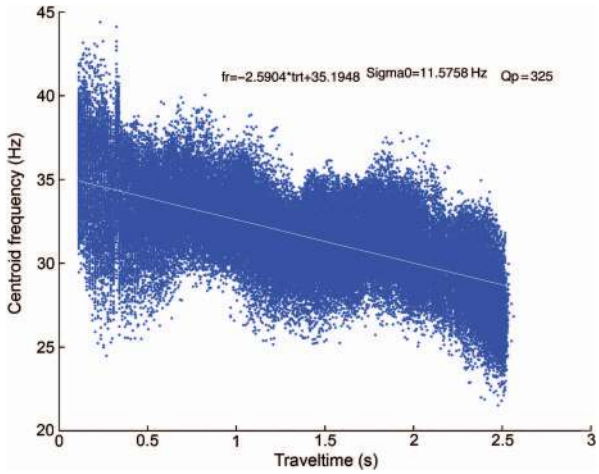

Figure 13. The centroid frequency of the first arrival versus first-arrival traveltime. The attenuation factor Q was estimated to be 325 by using the best-fit line shown as a solid white line.

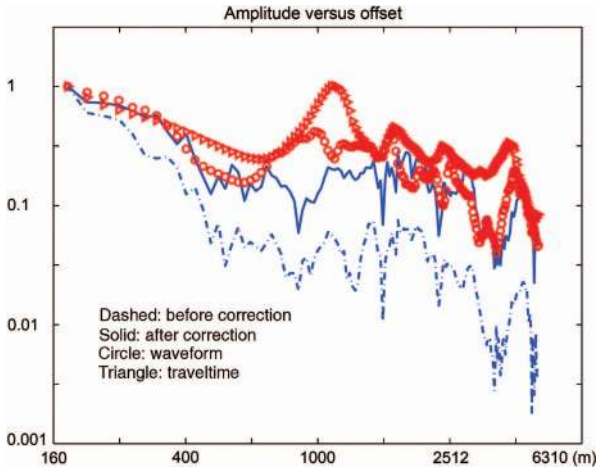

Figure 14. The log 10 amplitude (normalized by the amplitude at offset 160 m) versus log 10 offset for shot 663. The amplitudes calculated from the waveform tomogram (circle) correlate better with the corrected amplitudes (solid) than with those calculated from the traveltime tomogram (triangle). Compared to the uncorrected amplitudes and those obtained by the waveform tomogram, it can be seen that attenuation correction is important for EWT.

shot gathers were corrected. Figure 13 shows the plot of centroid frequency f_r versus traveltime t of the first arrival, and the Q value was estimated to be about 325. The correction $1/T(f)$ from equation 9 was then applied to the spectra from each trace to correct for the absorption effects.

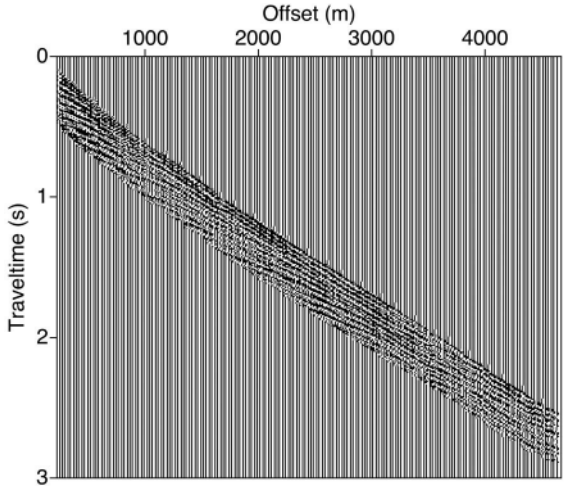

Figure 15. The CSG 663 after preprocessing. A time window of 100 ms after the first breaks was used for EWT.

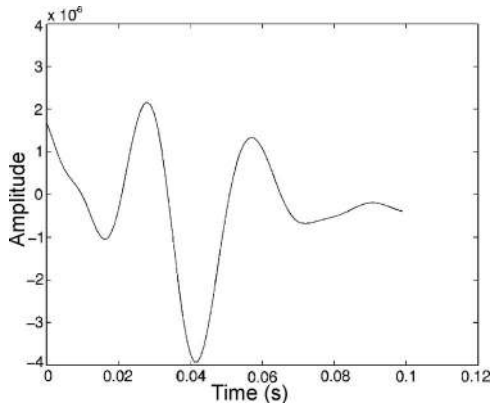

Figure 16. The inverted-source wavelet for shot 663.

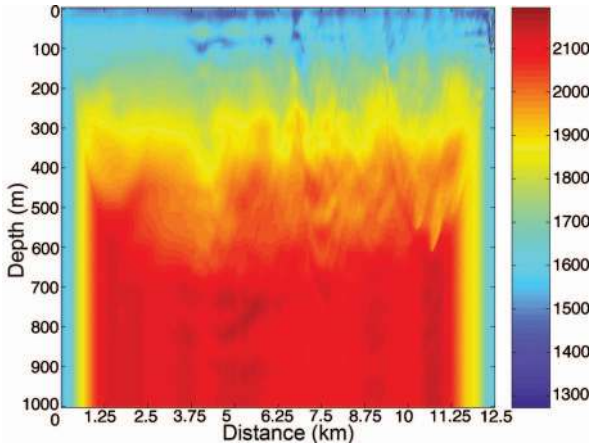

Figure 17. The waveform tomogram (velocity in m/s) after 14 iterations.

Figure 14 shows the first-arrival amplitude versus offset (AVO) curves with (solid) and without (dashed) attenuation correction. This plot indicates that an attenuation correction is required for EWT. Figure 15 shows CSG 663 after attenuation correction, muting with an early arrival time window of 100 ms and trace normalization.

- Using the traveltime-velocity tomogram as the initial model, the source wavelets were inverted, shown in Figure 16, by back projecting the near-offset waveform residuals. The waveform tomogram was obtained after 14 iterations, shown in Figure 17. Figure 18 shows the plot of waveform residual versus iterations, and Figure 19 shows the original data and the synthetic data calculated from the obtained waveform tomogram.
- Similarly, using the waveform tomogram, the EWT statics were

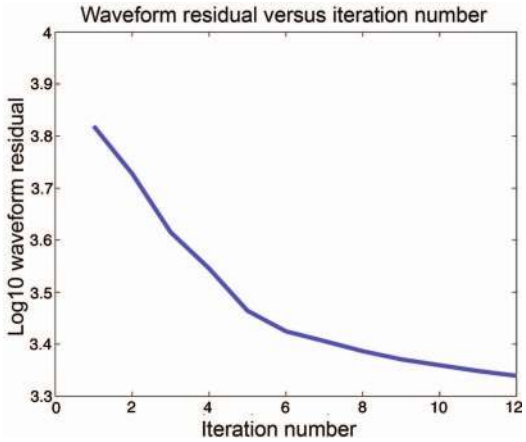

Figure 18. Waveform residual versus iteration number.

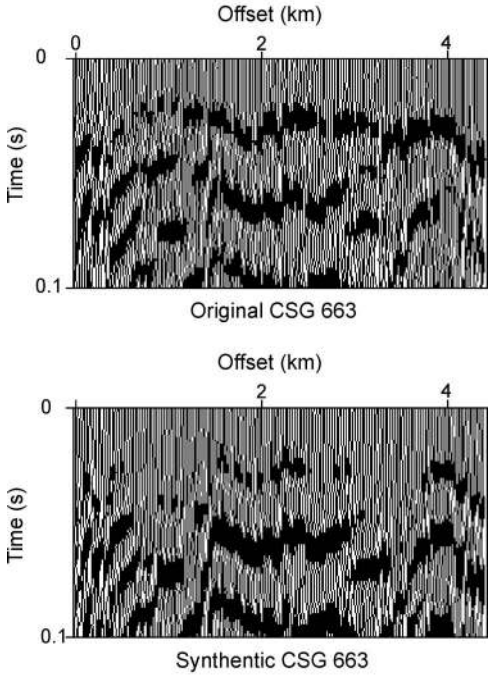

Figure 19. The original (top) and synthetic (bottom) CSG 663 aligned according to the first-arrival traveltimes.

calculated vertically down to the datum of 400 m and then upward to the surface, using a constant-substitute velocity. The reflection-residual statics were calculated by minimizing the time shifts between the adjacent traces after EWT statics and normal moveout (NMO) corrections. Figure 20 shows the stacked section after tomostatics + residual-statics corrections, which is improved compared with that shown in Figure 11, which used the traveltime tomogram. The improvement can be seen more clearly in the zoom views of Figure 21.

- The time-migration sections with the static corrections obtained from the EWT and traveltime tomograms are shown in Figure 22. Compared to the time-migration section using the traveltime tomogram, the EWT time-migration section shows moderate improvement around the A, B, and C labels marked in the figure. This suggests that the EWT tomogram provides the most accurate velocity structure.

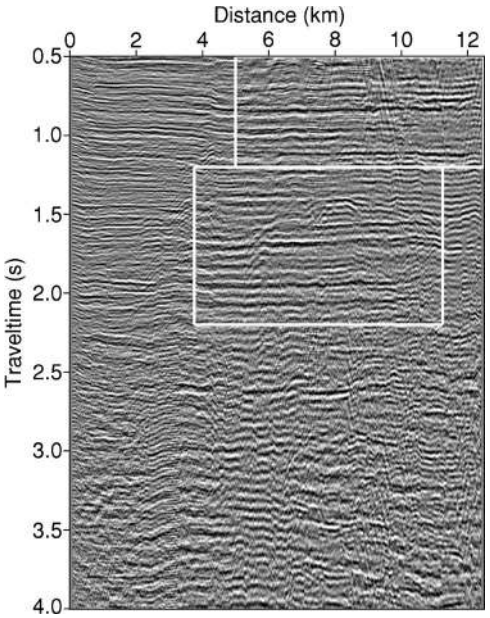

Figure 20. The stacked section after tomostatics correction and reflection-residual statics correction using the waveform tomogram. The reflectors are more clearly focused compared to those using the traveltime tomogram. The comparison between the stacked sections using the traveltime-tomogram and EWT-tomogram velocities is shown in Figure 21 for the zoom view of the two white boxes.

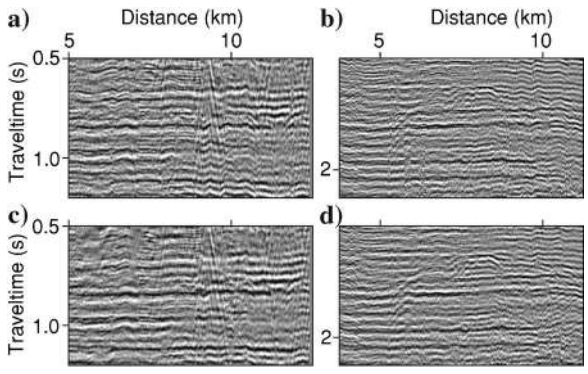

Figure 21. The zoom views for the upper white box in the stacked sections using the (a) traveltime tomogram and (c) EWT tomogram; and (b) and (d) show the zoom views for the lower white box in the same order.

2D near-surface refraction survey, Mapleton, Utah

The average interval of large earthquakes can be estimated by excavating trenches across normal faults (McCalpin, 1996). Trenching allows geologists to determine the location and shape of colluvial wedges, which are wedge-shaped deposits that accumulate at the base of a fault scarp following a surface-rupturing event. They are a characteristic geologic signature of an ancient dip-slip earthquake (McCalpin, 1996). Without excavating trenches, seismic imaging can be an efficient way to measure the colluvial wedges (Morey and Schuster, 1999; Sheley et al., 2003) of a fault. To demonstrate this idea, several 2D refraction surveys were carried out by Maike Buddensiek and Travis Crosby in September, 2002, before the Mapleton Megatrench was excavated by the URS Corporation in the summer of 2003 to image the colluvial wedges over the Wasatch fault near Mapleton, Utah. The EWT algorithm was applied to data collected from one of these surveys in which a total of 168 shot gathers and 168 traces per shot were used to invert for the velocity distribution. The geophone and shot spacings were 0.5 m with 0.5 ms time sampling and 1 s recording length.

Synthetic test

To test the resolving power and the reliability of EWT for this geometry, the trench log (geologic truth obtained after the trench was dug out) was used to construct a synthetic model (Figure 23) with six faults and one low-velocity zone. Synthetic seismograms were cal-

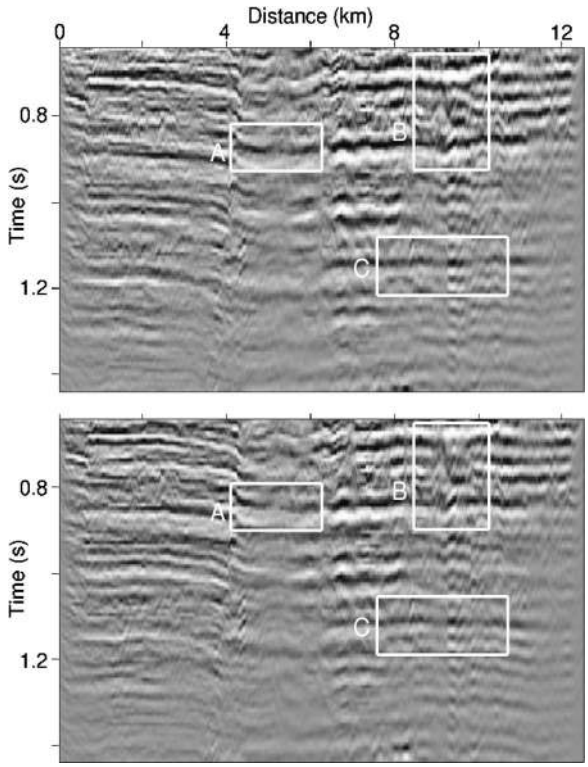

Figure 22. The time-migration section using the (top) waveform and (bottom) traveltime tomograms, respectively.

culated with the same forward-modeling code, the same geometry, and the same data sampling. First, the traveltime data were inverted with a fat-ray, traveltime-tomography method (Schuster and Quintus-Bosz, 1993), and the traveltime tomogram was obtained and shown in Figure 24 (top), in which six faults were imaged. Then, using the traveltime tomogram as the initial model, the EWT tomogram was obtained after 28 iterations and shown in Figure 24 (bottom). Compared with the traveltime tomogram, the EWT tomogram provided a much higher resolution of the faults and the low-velocity zones.

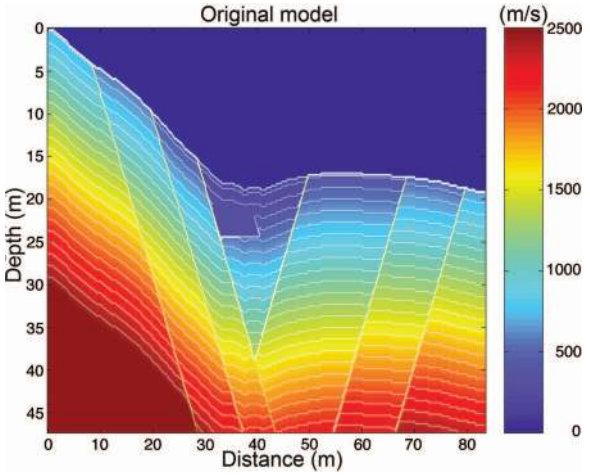

Figure 23. The contoured original model.

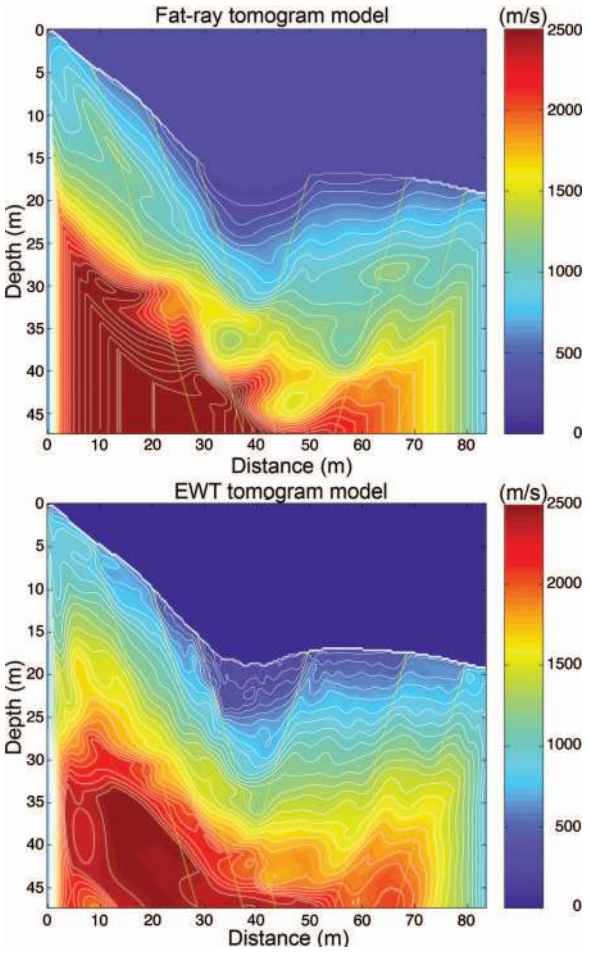

Figure 24. The contoured (top) fat-ray traveltime and (bottom) EWT tomograms.

Following the preprocessing steps, the Q value was estimated to be about 24, which is a typical value for near-surface surveys where the absorption is quite significant. The Q value is obtained from the line-fit to the graph, and the correction $1/T(f)$ was applied to the data spectra to correct for absorption effects. Figure 25 shows the corrected 49th CSG.

The Mapleton data were then processed with the same procedure described in the synthetic test. The starting-velocity model was obtained from a fat-ray, traveltime tomogram shown in Figure 26, in which the trench's benches are delineated with dark solid lines, and six faults and some colluvial wedges (low-velocity zones) are imaged. The source wavelets were estimated by stacking the first arrivals in the CSGs. Figure 27 shows the waveform tomogram after 10 iterations, and Figure 28 compares the original data with the synthetic data calculated from the obtained waveform tomogram. Com-

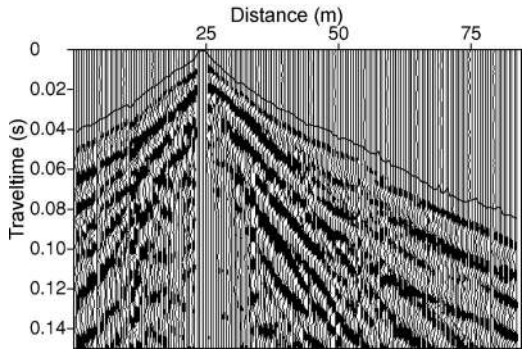

Figure 25. The 49th CSG after corrections. The solid line indicates the picked first-break traveltimes.

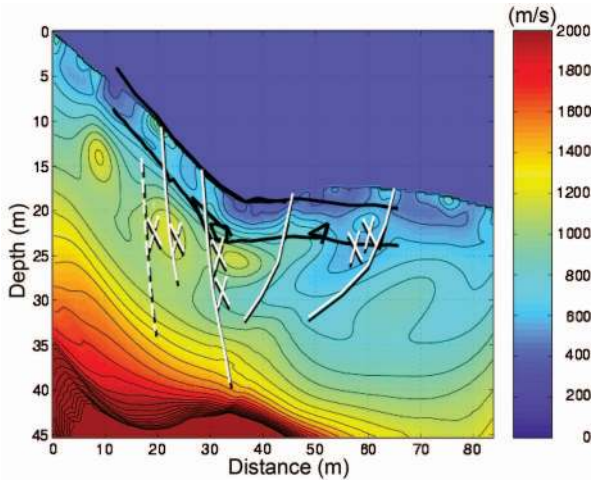

Figure 26. The fat-ray, traveltime-velocity tomogram for the Mapleton data. The dark solid lines delineated the location of the trench's benches, the white solid lines denote the faults observed from the trench log, the dashed lines are the interpreted possible faults, and X represents colluvial wedges observed in the excavated trench. The top surface, denoted by the uppermost dark solid line, is where 168 shots and geophones were evenly distributed.

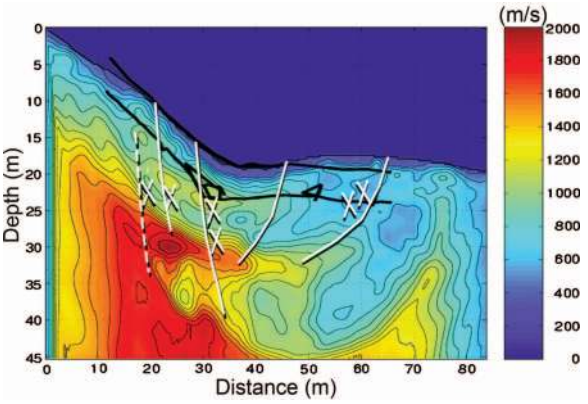

Figure 27. The waveform tomogram after 10 iterations. The dark solid lines delineated the trench's benches. Compared to the traveltime tomogram shown in Figure 26, the waveform tomogram produced several low-velocity zones that are more consistent with the location of colluvial wedges seen in the trench log.

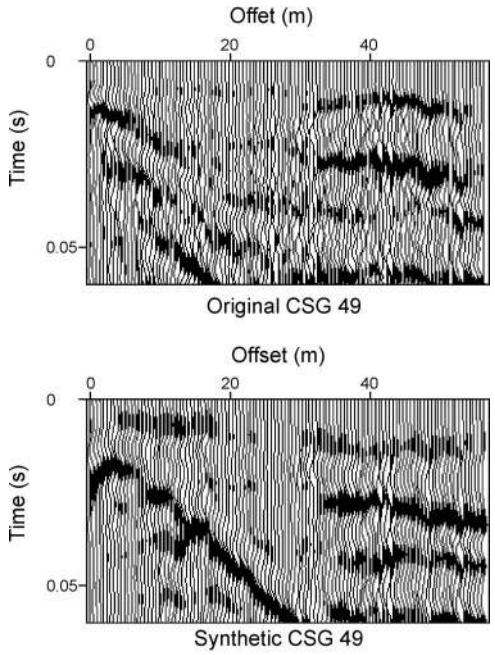

Figure 28. The original (top) and synthetic (bottom) CSG 49 aligned according to the first-arrival traveltimes.

pared to the traveltime tomogram in Figure 26, the waveform tomogram imaged six fault-like features, just as the traveltime tomogram, but it also provides more details. This is especially true for the low-velocity zones, which appear to match the locations of the trench-log colluvial wedges marked with *X*s in the tomograms. Further details about these data and numerous comparisons between the trench log, traveltime tomogram, and EWT tomogram are in Buddensiek (2004).

CONCLUSIONS

The EWT method is developed to invert for the subsurface velocity model from the early arrival waveforms that include the refraction arrivals. In comparison to the traveltime tomography, EWT does not require a high-frequency assumption and consequently can be applied to typical data from refraction surveys. The benefit is more accurate tomograms, as demonstrated by the synthetic data and the field data results (roughly double the spatial resolution for the Mapleton data). Using the EWT tomogram as a velocity model, more accurate tomostatics can be obtained, and the stacked section can be improved as indicated in the marine-data results. And, complex structures can be delineated more effectively as shown in the tomogram from the Mapleton trench data.

The drawback with EWT compared to traveltime tomography is that much more effort is needed to preprocess and invert the data. The computational cost of EWT is roughly 100–500 times that of traveltime tomography. The EWT method can be improved by (1) using a more realistic forward-modeling method to take into account 3D and nonacoustic phenomena such as viscoelastic-wave propagation; (2) using a more accurate estimate of the source wavelet; (3) using an improved objective function to mitigate the nonlinear problem; (4) using multigrid methods to attack the local minima problem; (5) improving the computational efficiency that is essential for 3D inversion; and (6) progressively extending the time window after fitting the early arrival waveforms to reconstruct the deeper structures.

ACKNOWLEDGMENTS

We thank the members of the University of Utah Tomography and Modeling/Migration (UTAM) Consortium for financial support. We thank WesternGeco for permission to publish the marine data. We thank Konstantin Osypov for early insights.

REFERENCES

Aki, K., and P. G. Richards, 2002, Quantitative seismology, 2nd ed.: University Science Books.
Barton, G., 1989, Elements of Green's functions and propagation: Oxford University Press, Inc.
Berenger, J., 1994, A perfectly matched layer for the absorption of electromagnetic waves: Journal of Computational Geophysics **114**, 185–200.
Bleistein, N., J. K. Cohen, and J. W. Stockwell, 2001, Mathematics of multidimensional seismic imaging, migration, and inversion: Springer-Verlag New York, Inc.
Buddensiek, Maike-L., 2004, Colluvial wedge imaging using traveltime tomography along the Wasatch fault near Mapleton, Utah: M.S. thesis, University of Utah.
Bunks, C., F. M. Saleck, S. Zaleski, and G. Chavent, 1995, Multiscale seismic waveform inversion: Geophysics, **60**, 1457–1473.
Červený, V., and E. Soares, 1992, Fresnel volume ray tracing: Geophysics, **57**, 902–915.
Chew, W., and Q. Liu, 1996, Perfectly matched layers for elastodynamics: A new absorbing boundary condition: Journal of Computational Acoustics **4**, 341–359.
Crase, E., C. Wideman, M. Noble, and A. Tarantola, 1992, Nonlinear elastic waveform inversion of land seismic reflection data: Journal of Geophysical Research, **97-B4**, 4685–4704.
Festa, G., and S. Nielsen, 2003, PML absorbing boundaries: Bulletin of the Seismological Society of America, **93**, 891–903.
Gauthier, O., J. Virieux, and A. Tarantola, 1986, Two-dimensional nonlinear inversion of seismic waveforms — Numerical results: Geophysics, **51**, 1387–1403.
Lailly, P., 1984, Migration methods: Partial but efficient solutions to the seismic inverse problem, *in* F. Santosa, Y. H. Pao, W. Symes, and C. Holland, eds., Inverse problems of acoustic and elastic waves: Society of Industrial and Applied Mathematics.
Levander, A., 1988, Fourth-order finite-difference P-SV seismograms: Geophysics, **53**, 1425–1437.
Liao, Q., and G. A. McMechan, 1996, Multifrequency viscoacoustic modeling and inversion: Geophysics, **61**, 1371–1378.
——, 1997, Tomographic imaging of velocity and Q with application to

crosswell seismic data from the Gypsy Pilot Site, Oklahoma: Geophysics, **62**, 1804–1811.
Luo, Y., and G. T. Schuster, 1991, Wave equation traveltime inversion: Geophysics, **56**, 645–653.
Marsden, D., 1993, Static corrections — A review, Part III: The Leading Edge, **12**, 210–216.
McCalpin, J. P., 1996, Paleoseismology: Academic Press Inc.
Mora, P. R., 1987, Nonlinear two-dimensional elastic inversion of multioffset seismic data: Geophysics, **52**, 1211–1228.
——–, 1988, Elastic wavefield inversion of reflection and transmission data: Geophysics, **53**, 750–759.
Morey, D., and G. T. Schuster, 1999, Paleoseismicity of the Oquirrh fault, Utah from shallow seismic tomography: Geophysical Journal International, **138**, 25–35.
Nemeth, T., E. Normark, and F. Qin, 1997, Dynamic smoothing in cross-well traveltime tomography: Geophysics, **62**, 168–176.
Nocedal, J., and S. J. Wright, 1999, Numerical optimization: Springer Series in Operations Research and Financial Engineering, Springer-Verlag New York, Inc.
Pratt, R. G., 1990, Inverse theory applied to multi-source cross-hole tomography. Part I: Acoustic wave-equation method: Geophysical Prospecting, **38**, 287–310.
Pratt, R. G., C. Shin, and G. J. Hicks, 1998, Gauss-Newton and full Newton methods in frequency space seismic waveform inversion: Geophysical Journal International, **133**, 341–362.
Pratt, R. G., Z.-M. Song, P. Williamson, and M. Warner, 1996, Two-dimensional velocity models from wide-angle seismic data by wavefield inversion: Geophysical Journal International, **124**, 323–340.
Pratt, R. G., and M. H. Worthington, 1988, The application of diffraction tomography to cross-hole seismic data: Geophysics, **53**, 1284–1294.
Rothman, D., 1985, Nonlinear inversion, statistical mechanics, and residual statics estimation: Geophysics, **50**, 2784–2796.
——–, 1986, Automatic estimation of large residual statics corrections: Geophysics, **51**, 332–346.
Schuster, G. T., and A. Quintus-Bosz, 1993, Wavepath eikonal traveltime inversion: Theory: Geophysics, **58**, 1314–1323.
Sheley, D., J. Yu, R. He, G. T. Schuster, T. Crosby, M. Zhou, and J. Giacoma, 2003, 2-D seismic trenching of colluvial wadges and faults: Tectonophysics, **368**, 51–69.
Shipp, R. M., and S. C. Singh, 2002, Two-dimensional full wavefield inversion of wide-aperture marine seismic streamer data: Geophysical Journal International, **151**, 325–344.
Taner, M. T., D. E. Wagner, E. Baysal, and L. Lu, 1998, A unified method for 2-D and 3-D refraction statics: Geophysics, **63**, 260–274.
Tarantola, A., 1984, Inversion of seismic reflection data in the acoustic approximation: Geophysics, **49**, 1259–1266.
——–, 1986, A strategy for nonlinear elastic inversion of seismic reflection data: Geophysics, **51**, 1893–1903.
——–, 1987, Inverse problem theory: Methods for data fitting and parameter estimation: Elsevier Science Publishing Company, Inc.
Vasco, D. W., J. E. Peterson, and E. L. Majer, 1995, Beyond ray tomography: Wavepaths and Fresnel volumes: Geophysics, **60**, 1790–1804.
Wang, Y., 1995, Preliminary results for viscoelastic WTW inversion of cross-well data: University of Utah Tomography and Modeling/Migration Development Project, Annual Report, 217–231.
Wilson, W. G., W. G. Laidlaw, and K. Vasudevan, 1994, Residual statics estimation using the genetic algorithm: Geophysics, **59**, 766–774.
Woodward, M. J., 1992, Wave-equation tomography: Geophysics, **57**, 15–26.
Zeng, Y., J. Q. He, and Q. Liu, 2001, The application of the perfectly matched layer in numerical modeling of wave propagation in poroelastic media: Geophysics, **66**, 1258–1266.
Zhang, J., 1996, Nonlinear refraction and reflection traveltime tomography: Ph.D. thesis, Massachusetts Institute of Technology.
Zhou, C., W. Cai, Y. Luo, G. T. Schuster, and S. Hassanzadeh, 1995, Acoustic wave-equation traveltime and waveform inversion of crosshole seismic data: Geophysics, **60**, 765–773.
Zhou, C., G. T. Schuster, S. Hassanzadeh, and J. M. Harris, 1997, Elastic wave equation traveltime and waveform inversion of crosswell data: Geophysics, **62**, 853–868.
Zhu, X., D. P. Sixta, and B. G. Angstman, 1992, Tomo-statics: Turning-ray tomography + static corrections: The Leading Edge, **11**, 15–23.